Available online at www.sciencedirect.com
SCIENCE DIRECT®
Journal of Solid State Chemistry 171 (2003) 123–132
JOURNAL OF SOLID STATE CHEMISTRY
http://elsevier.com/locate/jssc

Confinement of electron–phonon interaction on luminescence dynamics in nanophosphors of Er^{3+}:Y_2O_2S

G.K. Liu,[a,*] X.Y. Chen,[a] H.Z. Zhuang,[a] S. Li,[b] and R.S. Niedbala[b]

[a] *Chemistry Division, Argonne National Laboratory, Argonne, IL 60439, USA*
[b] *OraSure Technologies, Inc. 150 Webster St., Bethlehem, PA 18015, USA*

Received 6 June 2002; received in revised form 20 July 2002; accepted 13 November 2002

Abstract

Observation of an anomalous thermalization effect induced by optical excitation of Er^{3+} in nanocrystals of Y_2O_2S was recently reported (Liu et al. Nano Lett. 2 (2002) 535). Due to the absence of low-energy phonon modes in nanocrystals, the nonradiative relaxation between crystal field levels of Er^{3+} is significantly diminished, whereas this confinement effect on high-energy phonon relaxation and thermalization is negligible. It is also shown that absorption line broadening for Er^{3+} ions in the surface layer of the nanoparticles enables coincident excitation of Er^{3+} ions at defect and intrinsic sites. As a result of the combined excitation and relaxation processes, Er^{3+} population accumulates in the upper crystal field levels of the $^4I_{15/2}$ ground state; and the intensity of hot bands originating from these levels increases abruptly as temperature decreases below 7 K. This anomalous thermalization effect is interpreted satisfactorily based on calculations of temperature-dependent multiphonon relaxation rates in nanocrystals of confined phonon modes.

Keywords: Nanocrystals; Quantum confinement; Density of phonon states; Electron–phonon interaction; Er^{3+}; Nonradiative relaxation; Anomalous thermalization

1. Introduction

It is now well known that size-dependent quantum confinement has significant effects on both radiative and nonradiative electronic transitions in nanoparticles, and that modifying and controlling structure at the nanometer scale may induce novel properties for potential applications. For rare-earth (RE) ions doped into nanocrystalline materials in which they have localized electronic states, confinement effects may be induced by inter-ionic electronic interactions and, particularly, through electron–phonon interactions [1–7]. Phonon density of states (PDOS) are modified in nanocrystals because of the finite particle size. As a result, the acoustic-phonon spectrum becomes discrete with a cutoff frequency in the low energy side [1,2,8]. Because the low-frequency phonons contribute most effectively to the nonradiative relaxation between the closely spaced crystal-field levels, lack of low-frequency phonon modes in nanocrystals is expected to drastically change the spectra and luminescence dynamics of optically active ions. Meltzer et al. [2,3] observed that the temperature dependence of the linewidth of spectral holes burned in the $^7F_0 \rightarrow {}^5D_0$ transition of Eu^{3+} ions in Eu_2O_3 nanoparticles was strongly weakened from $\sim T^7$ to T^3. Yang et al. reported that the lifetime of the 2nd Stark level of the $^5D_1$ multiplet of Eu^{3+} in Y_2O_3 nanocrystals showed an increase from 220 ns to 27 μs compared to the bulk crystal [4–6]. Liu et al. [1] recently reported an anomalous thermalization effect induced by optical excitation of Er^{3+} ions in nanocrystals of Y_2O_2S. Due to elimination of direct phonon relaxation between the Er^{3+} crystal field levels in the $^4I_{15/2}$ ground state, intensities of unusually strong and sharp hot bands increase as temperature decreases below 7 K. Similar effect was also noticed but left unexplained for Eu^{3+} in Eu_2O_3 nanocrystals, where the broad hot bands of the transition $^7F_1 \rightarrow {}^5D_1$ were observed in excitation spectra at 12 K [7].

In this paper we provide a detailed analysis of the spectra and excited state dynamics of Er^{3+} in Y_2O_2S

*Corresponding author. Fax: +1-630-252-7501.
E-mail address: gkliu@anl.gov (G.K. Liu).

0022-4596/03/$ - see front matter © 2003 Published by Elsevier Science (USA).
doi:10.1016/S0022-4596(02)00195-0

nanocrystals. Based on calculations of PDOS and various relaxation and thermalization mechanisms, experimental spectra are quantitatively modeled as a function of temperature and pumping intensity.

2. Experimental procedures

The nanocrystals were synthesized using flame spray pyrolysis (FSP). Descriptions of the general procedure of using FSP for nanoparticle formation have been published [9,10]. The method is based on the rapid combustion of a flammable precursor aerosol. For the nanocrystals of Y_2O_3 that contain 2–4% Er^{3+} and 2–8% Yb^{3+}, metal carboxylates in the desired stoichiometry are dissolved in ethanol to give a solution with a ceramic yield of ~2.5 wt% after pyrolysis. The solution is pumped through an atomizer into a quartz combustion chamber, where the fine aerosol is immediately ignited by a methane-fueled pilot torch. Combustion occurs at 1600–2000°C, completely oxidizing the organic portion of the precursor and converting the metals to nanoparticulate oxide "smoke". Rapid quenching of the nanoparticles (to ~500°C in <1 s) occurs as the product and waste gases are drawn from the combustion chamber by exhaust fans. The nanopowders are collected as the exhaust stream flows through a series of electrostatic precipitation (ESP) tubes biased at 10 kV DC. Average collection efficiencies are ~70%. To obtain Y_2O_2S:Er^{3+}(Yb^{3+}) nanocrystals, a fluidized bed sulfiding process (FBS) was conducted. Y_2O_3:Er^{3+}(Yb^{3+}) powders were sulfided in a quartz fluidized bed reactor at 850°C under a stream of $H_2S/H_2O/N_2$ gas mixture in a nitrogen atmosphere. The structure of the obtained nanocrystals was characterized by powder X-ray diffraction and transmission electron microscopy (TEM). X-ray diffraction patterns of the samples were compared with standard JCPDS files to identify crystalline phases. The TEM images show that most particles have sizes between 10 and 50 nm.

Excitation and emission spectra were induced by a pulsed dye laser, which provides a pulse width of 5 ns and a repetition rate of 10 Hz with a tunable range from 470 to 560 nm. The luminescence was dispersed by a 1-m monochrometer and detected with a cooled RCA-C31034 photomultiplier. The spectra were recorded by using a gate-controlled boxcar. The laser beam at the sample surface had a beam diameter of ~3 mm. The incident laser power was adjusted by inserting neutral density filters with different absorbance. In our experiments, the crystalline powders of 10–50 nm crystals and 400 nm (bulk) crystals were sealed off in quartz cells filled with 1 Torr of helium gas. Two samples were mounted on the same sample holder in the cryostat for comparative studies. For measurements at temperatures below 4 K, liquid helium was accumulated in the sample chamber and the vapor gas was pumped to control the liquid temperature. The fluorescence emission was detected using a boxcar integrator that averaged the fluorescence signal from a cooled PMT. Typically, time-resolved fluorescence was detected with 3 μs gate and 1 μs delay from the pumping laser pulse. The spectrometer bandwidth was set approximately at 0.5 cm^{-1}.

3. Results and discussion

3.1. Crystal-field levels of Er^{3+}:Y_2O_2S

The experiments were conducted on the nanocrysals of Y_2O_2S that contain 2% Er^{3+} ions. Although the Y_2O_2S crystals were co-doped with Er^{3+} and Yb^{3+}, the excitation and emission energies of Er^{3+} are above the $4f^{13}$ energy levels of Yb^{3+}, and the Yb^{3+} charge transfer bands are above the energy level of the $^4F_{7/2}$ state of Er^{3+}, therefore, the Yb^{3+} ions have no influence to the present work. The excitation and emission spectra of Er^{3+} in Y_2O_2S nanocrystals and 400 nm crystals were recorded at liquid helium temperature. Some crystal-field levels below the manifold $^4F_{7/2}$ are identified and listed in Table 1. Our results show that there is no observable difference in the peak positions in the spectra between nanocrystals and bulk crystals, which indicate that the local crystalline structure remains similar for Er^{3+} ions in the two samples. Some of the crystal-field levels identified in the present work differ from that reported 30 years ago [11], particularly for the crystal field splitting in the $^4I_{15/2}$ ground state. Apparently, several crystal field levels of the ground state could be incorrectly assigned in the previous work.

3.2. Evidence of anomalous thermalization effect

The excitation spectra of the bulk (400 nm) and nanocrystalline Er^{3+}:Y_2O_2S samples due to the $^4I_{15/2} \rightarrow {}^4F_{7/2}$ transition at 2.6 K are shown in Fig. 1. A number of unusually strong hot bands appear in the spectrum of the nanoparticle sample, whereas the excitation of Er^{3+} in the bulk sample is only from the lowest level of the $^4I_{15/2}$ ground state. According to the Boltzmann distribution of Er^{3+} population in the crystal field levels of $^4I_{15/2}$, Er^{3+} ions should populate only the lowest level at 2.6 K. The Boltzmann factors at 2.6 K for the 2nd and 3rd crystal field levels are calculated to be 3.2×10^{-4}% and 1.8×10^{-9}%, respectively. Hence under normal conditions, the excitation spectra are expected to be exactly like that of the bulk sample with only four sharp absorption peaks arising from the lowest level of the $^4I_{15/2}$ ground state to the four crystal field levels (a–d) of the $^4F_{7/2}$ excited multiplet, which are indicated by the vertical lines in Fig. 1. In addition to the four transitions from the

Table 1
Partial energy levels of Er^{3+} in Y_2O_2S nanocrystals at 3 K

Multiplet	Energy (cm^{-1})								Ref.
$^4I_{15/2}$	0	23	45	210	224	249	388	410	This work
	0	23	46	102	174	220	262	419	[11]
$^4I_{13/2}$	6476	6479	6499	6584	6609	6615	6644		This work
	6478	6497	6520	6587	6637	6665	6692		[11]
$^4S_{3/2}$	18,248	18,263							This work
	18,236	18,250							[11]
$^2H_{11/2}$	18,955	18,972	18,987	19,086	19,106	19,127			This work
	18,930	18,941	18,959	19,082	19,104	19,119			[11]
$^4F_{7/2}$	20,333	20,390	20,400	20,415					This work
	20,320	20,382	20,392	20,404					[11]

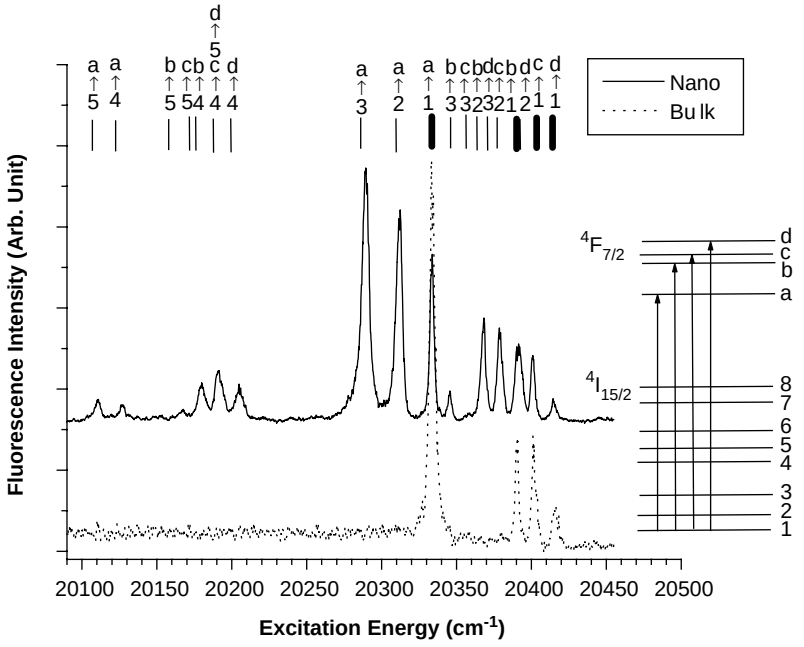

Fig. 1. Excitation spectra of Er^{3+} in 10–40 nm diameters (solid curve) and 400 nm diameters (dashed curve) nanocrystals of Y_2O_2S at 2.6 K. The optical transition is from the $^4I_{15/2}$ ground state to the $^4F_{7/2}$ excited state while emission from the $^4S_{3/2}$ excited state at 18,248 cm^{-1} is monitored. The vertical lines indicate the electronic transitions from the crystal field levels of ground state to that of the excited state. The fluorescence emission was detected using a boxcar integrator that averaged the fluorescence signal from a cooled PMT with 3 μs gate and 1 μs delay from the laser pulse. The spectrometer bandwidth was set approximately at 0.5 cm^{-1}.

lowest level of the ground state, we are able to assign all the hot bands in the spectrum of Er^{3+} in the nanoparticle sample. The positions of the hot bands are coincident exactly with the energy levels determined from the emission spectra (Table 1).

It is novel that the hot bands could originate from the upper Stark levels of the $^4I_{15/2}$ ground state at 2.6 K with energy gaps up to 224 cm^{-1} ($5 \rightarrow a$). More curiously, many hot bands, such as 2, $3 \rightarrow a$, b lines, are much stronger than the normal lines from the ground level; the hot bands are much narrower than a normal hot band. Similar hot bands were observed when the laser excitation was tuned to the $^2H_{11/2}$ multiplet with energies between 18,955 and 19,127 cm^{-1}.

In the emission spectra, we observed the anomalous hot bands due to the Er^{3+} population in the upper levels of the $^4S_{3/2}$ emitting state. Again, the hot bands appear in the emission spectrum of Er^{3+} in the nanoparticle sample, not in the bulk sample, while both samples were in liquid helium with temperature below 3 K. Fig. 2

shows the emission spectra of the two samples with laser excitation into the lowest level of the $^4F_{7/2}$ excited state at 3 K. Three hot bands in the spectrum of Er^{3+} in the nanoparticle sample are marked with $b \rightarrow 1, 2, 3$, respectively.

3.3. Temperature and power dependence

To obtain a better understanding of the mechanism of anomalous thermalization in Er^{3+}:Y_2O_2S nanocrystals, temperature and power dependence of fluorescence intensity in the excitation spectra were investigated. Here we focus our attention on the three representative excitation peaks at 20,333, 20,310, and 20,288 cm^{-1}, which correspond to the transitions of $^4I_{15/2}$ (1), (2) and (3) $\rightarrow$ $^4F_{7/2}$ (a), respectively (see Fig. 1).

The influence of normal heating of samples in laser excitation was excluded not only by comparing the spectra from bulk and nanoparticle samples at the same condition. It was also observed that, when temperature was varied between 3 and 10 K, the hot bands in the excitation spectrum had a very drastic and unusual response. First, the hot bands were saturated below 5 K with modest laser intensity; and the hot bands diminished abruptly when T increased from 5 to 6 K. Then, all hot bands except those from the level 2 vanished completely near 7 K. Finally, the hot bands increased with temperature above 10 K, showing a normal behavior described by Boltzmann thermal distribution. Fig. 3(b) and (c) show the temperature dependence of the integrated intensities of the 2, 3 $\rightarrow a$ hot bands at two different laser intensities in comparison with that of the $1 \rightarrow a$ line of the excitation from the ground level (Fig. 3a). The results shown in Fig. 3 suggest that, (1) there is a transition temperature ($\sim$7 K) below which anomalous thermalization occurs; (2) the hot band reaches saturation below 5 K at higher laser intensities (Fig. 3b and c); however, the anomalous thermalization still occurs at low laser pulse intensity less than 5 kW/cm^2 as long as the excitation from the lowest level is observable; (3) as shown in Fig. 3(a), the intensity of the excitation from the lowest level in the ground state decreases as the hot band intensity increases, indicating that the hot bands are indeed due to the Er^{3+} population in the upper levels of the ground state.

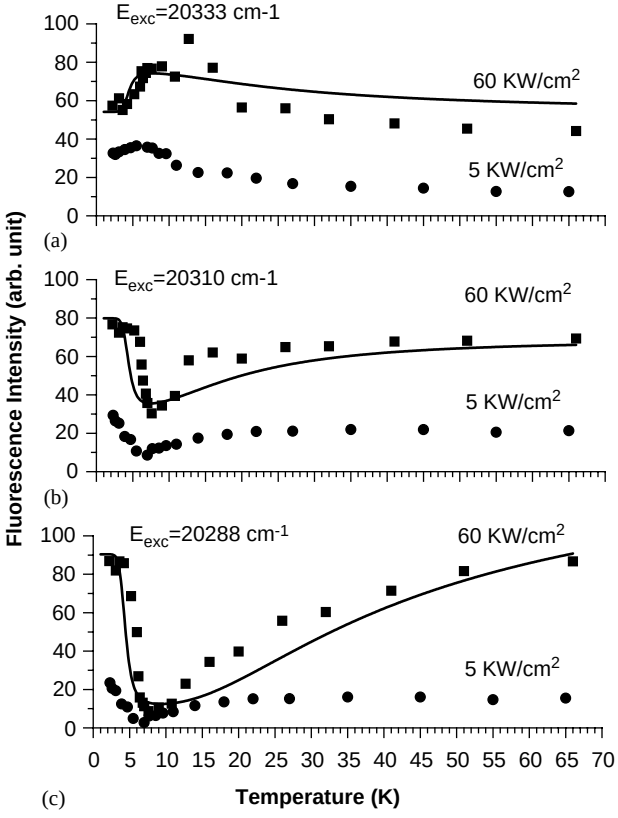

Fig. 3. Temperature dependence of integrated intensity of the excitation spectra under pump intensities of 60 and 5 KW/cm^2 for, (a) $^4I_{15/2}(1) \rightarrow {}^4F_{7/2}(a)$ (20,333 cm^{-1}); (b) $^4I_{15/2}(2) \rightarrow {}^4F_{7/2}(a)$ (20,310 cm^{-1}); and (c) $^4I_{15/2}(3) \rightarrow {}^4F_{7/2}(a)$ (20,288 cm^{-1}). The solid curves are calculated using Eqs. (3)–(7).

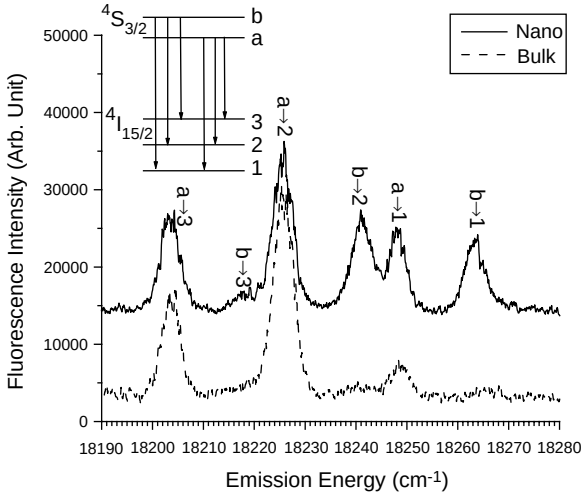

Fig. 2. Comparison of the emission spectra of the transitions $^4S_{3/2} \rightarrow {}^4I_{15/2}$ in the nanocrystalline and bulk Er^{3+}:Y_2O_2S at 3 K. The excitation was to the lowest level of the $^4F_{7/2}$ state at 20,333 cm^{-1}, and other experimental conditions were the same as that for Fig. 1.

The pump intensity dependences of integrated intensity of the three excitation bands $^4I_{15/2}(1,2,3) \rightarrow {}^4F_{7/2}(a)$ in Er^{3+}:Y_2O_2S nanocrystals at 3 and 20 K were measured and shown in Fig. 4(a) and (b), respectively. As normally expected, the integrated intensity of each excitation band is proportional to the pump intensity, which is the case of 20 K. But at 3 K, the pump intensity dependence becomes quite different. As shown in Fig. 4(a), the fluorescence intensity of all three bands exhibits a nonlinear dependence on the pump laser intensity. At low pump intensities ($<$11 kW/cm^2, see the inset of Fig. 4a), the power index, $\alpha(I_{\text{fluo.}} \propto I^{\alpha}_{\text{pump}})$, is

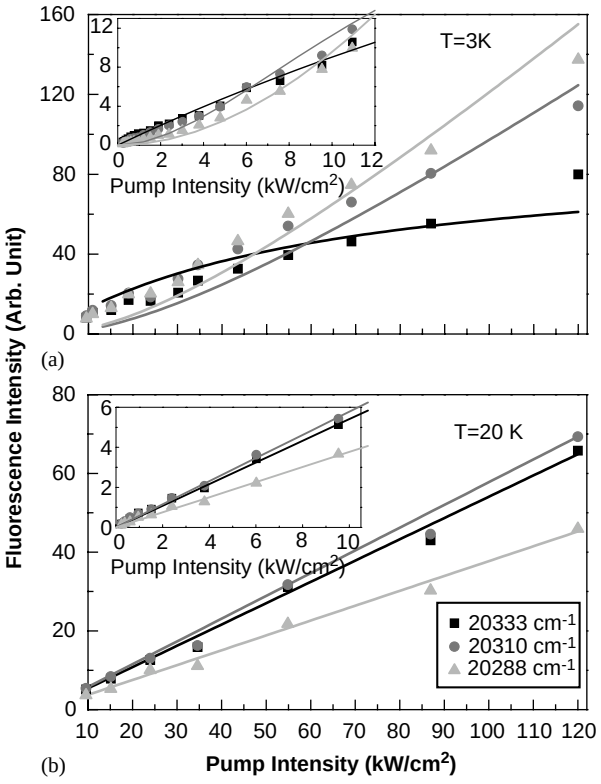

Fig. 4. Laser intensity dependence of the integrated intensity of the 3 excitation lines of $^4I_{15/2}(1,2,3)\rightarrow{}^4F_{7/2}(a)$ in Er^{3+}:Y_2O_2S nanocrystals at (a) 3 K, (b) 20 K, respectively. Insets are enlargement for the parts of low pump intensity (below 12 kW/cm^2). The scattering points are experimental data, and the solid curves are calculated results.

approximately 1.4 for the excitation at 20,288 cm^{-1} and 1.2 for the excitation at 20,310 cm^{-1}. The fluorescence intensity excited through the $^4I_{15/2}$ to $^7F_{7/2}$ (a) excitation with laser energy at 20,333 cm^{-1} shows a saturation tendency with an increase in pump power, and its power index is approximately 0.88. At 20 K, all excitation bands show a linear dependence on the pump intensities from 10 to 120 kW/cm^2.

3.4. Effect of surface defects

Except for the novel behavior of the hot bands in the nanocrystals, the characteristics of the Er^{3+} crystal field spectrum are well understood [11,12]. In crystals, the localized 4f electrons of rare-earth ions are weakly coupled to the lattice field, so that electronic transitions between the crystal field levels within the 4f configuration have very sharp spectra. At liquid helium temperatures, a typical line width of the $4f-4f$ transitions is only of the order of 1 cm^{-1}. Due to inhomogeneous line broadening, the line width of 4f spectra increases to 100 cm^{-1} or broader in glasses and structure-disordered solids. In nanocrystals, the influence of lattice defects and contamination of hydrous species in the considerably large area of surface layer is not negligible. They induce inhomogeneous broadening like that in glasses, whereas in the particle center ions should have unperturbed crystalline lattice environment. Without selective excitation and fluorescence line narrowing, the 4f spectra from nanocrystals include contributions from ions in the surface layer as well as from the ions in the particle center. In Fig. 5 the broad feature in the spectrum of the nanocrystals is indicated as the area below the dashed horizontal line, and it is attributed to the Er^{3+} ions at defect sites in the surface layer, whereas the sharp lines are due to the ions in the center.

The broad-band excitation, which has intensity less than 10% of the intrinsic bands, is essential for understanding the complicated luminescence dynamics and anomalous thermalization effect. In Fig. 5, the spectrum indicates that the hot bands originated from the upper crystal field levels are overlapped "accidentally" with the excitation of some defect sites from the lowest level in the ground state. In our experiments when the laser was tuned to induce a resonant transition apparently from an upper level of the ground state which was initially empty at liquid helium temperature, it actually pumped the Er^{3+} ions at defect sites from the ground level with excitation energy accidentally at the same level as that of the Er^{3+} ions at the intrinsic site from the upper crystal field levels. Through energy transfer and cascade emission of phonons, which occur efficiently in less than 5 ns after the laser pulse, the relaxation of an excited Er^{3+} ion at a defect site may result in populating more than one Er^{3+} ion in the upper levels of the ground state. Through this type of cross-relaxation, the empty levels in the $^4I_{15/2}$ ground multiplet are populated at liquid helium temperature. The Er^{3+} ions in these upper levels can be excited by the same laser pulse. Depending on the rate of nonradiative

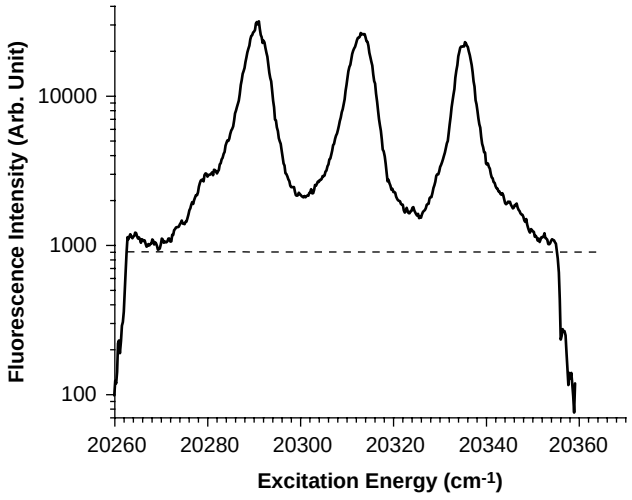

Fig. 5. Contribution of Er $^{3+}$ ions in the surface layer versus that in the center of the nanocrystals. The excitation spectrum of the transitions $^4I_{15/2}(1,2,3)\rightarrow{}^4F_{7/2}(a)$ in Er^{3+}:Y_2O_2S nanocrystals was recorded at 2.2 K.

phonon relaxation of ions in the upper levels, observation of hot bands is possible. This effect is similar to a photon avalanche [13,14] except that a threshold is not observed in the present work.

4. Analyses

4.1. Confined phonon density of states

In normal conditions, direct phonon relaxation in solids is very efficient and thermal population of ions in upper electronic states obeys Boltzmann distribution: $n = n_0 \exp(-\Delta E/kT)$. Therefore, no hot bands are observed from the states with energy gap ΔE much higher than kT. This is what we observed in the sample of 400-nm crystals. However, the Debye approximation of continuous distribution of PDOS is no longer valid for nanocrystals, in which vibrational modes become discrete, and no phonon modes exist below a cutoff energy in the low-energy side of density of state [8]. As a result, nonradiative relaxation and thermalization are restricted at certain electronic states because of the absence in phonon modes. Particularly, multi-phonon relaxation, which has a much higher rate than that of the one phonon rate, is eliminated between the states separated by a small energy gap. The vibrational modes of a finite sphere were analyzed previously by Lamb [15] and Tamura et al. [8]. In order to reveal the size dependence of phonon modes, we have calculated the PDOS for the low-energy phonon modes in nanocrystals of Y_2O_2S, which have a space group D_{3d}^3, and unit cell lattice constants of $a = 3.78$ Å, $c = 6.56$ Å. The Er^{3+} ions substitute Y^{3+} positions with a site symmetry of C_{3v} [16].

The reduced eigenvalues of acoustic phonon modes were calculated numerically and the $(2l+1)$-fold degeneracy of the lth state and two vibrational modes were taken into account in the evaluation of the PDOS. A stress-free boundary condition at the surface and finiteness conditions on both elastic displacements and stresses at the center are assumed in our calculation. These boundary conditions yield the spheroidal modes and torsional modes, which are determined by the following equations [8]:

$$2\left\{\eta^2 + (l-1)(l+2)\left[\eta\frac{j_{l+1}(\eta)}{j_l(\eta)} - (l+1)\right]\right\}\xi\frac{j_{l+1}(\xi)}{j_l(\xi)} - \frac{1}{2}\eta^4 + [\eta^2 - 2l(l-1)(l+2)] \times \eta\frac{j_{l+1}(\eta)}{j_l(\eta)} + (l-1)(2l+1)\eta^2 = 0, \quad (1)$$

$$\frac{\mathrm{d}}{\mathrm{d}\eta}\frac{j_l(\eta)}{\eta} = 0. \quad (2)$$

where J_l is the lth order spherical Bessel function, and $\xi = \omega R/v_l$ and $\eta = \omega R/v_t$. The parameters v_l and v_t are the sound velocities of the longitudinal and transverse modes, respectively, ω is phonon frequency, R is radius of the particle. Based on Eqs. (1) and (2), the phonon density of states can be calculated for a given system with known value of crystal size and sound velocities.

The calculated PDOS in the Y_2O_2S crystals with diameters of 20 and 40 nm are plotted in Fig. 6(a) and (b), respectively. It is clearly shown that the phonon modes with energy less than 200 cm^{-1} are reduced significantly, and there are no phonon modes below 24 cm^{-1} in the 20 nm crystals, whereas the cutoff energy reduces to 13 cm^{-1} for 40-nm crystals.

4.2. Nonradiative relaxation and thermalization in a nanoparticle

The anomalous thermalization phenomena we observed in the nanoparticels must be closely related to the size confinement effects on the nonradiative relaxation through electron–phonon interactions. In nanoparticles in which the low energy phonon modes are absent, direct phonon relaxation between the levels with energy gap less than the cutoff phonon frequency is completely suppressed. According to our calculation of phonon density of states, a cutoff frequency 24 cm^{-1} in the 20 nm particles should prevent nonradiative relaxation between the Er^{3+} crystal field levels with gaps less than 24 cm^{-1} which include the first two levels above the ground level of $^4I_{15/2}$ and the two levels of the $^4S_{3/2}$ excited state. The multiphonon relaxation between the closely spaced energy levels is even more improbable than one-phonon relaxation [17]. At low temperature, the rate of N phonon relaxation may be expressed approximately as

$$W(N\hbar\omega) = W_e(1 - \mathrm{e}^{-\hbar\omega/kT})^{-N}, \quad (3)$$

where $N = \Delta E/\hbar\omega$ with ΔE being the energy gap between the two crystal field levels.

Since the direct one and multiphonon relaxation processes between the closely spaced energy levels are greatly restrained in nanocrystals, the mechanism of 2-phonon Raman process becomes dominant, which is also strongly dependent on temperature [18,19]. It is well known that 2-phonon Raman process contributes mainly to the thermal broadening and line shift when temperature above 70 K in bulk materials. The 2-phonon Raman emission process between neighboring electronic energy levels depopulates the ions of the upper level, while 2-phonon Raman absorption process populates the upper level.

Because the size confinement has little effect on nonradiative relaxation and thermalization between the electronic states with energy gaps near or higher than the Debye energy of the lattice, we may anticipate that, after initial excitation by a 5-ns laser pulse, phonons of various energies may be created while the

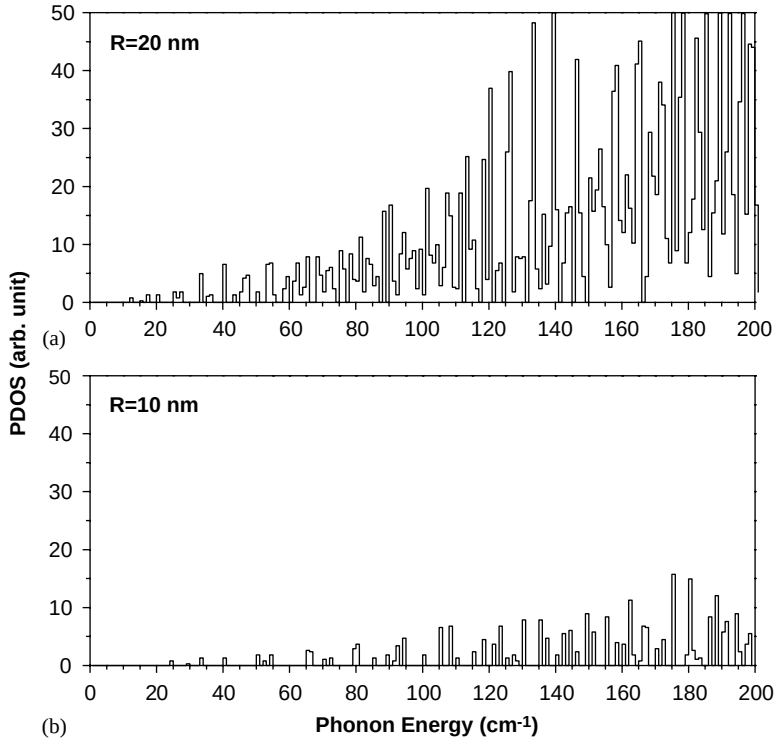

Fig. 6. Calculated phonon density of states in (a) 20 nm and (b) 40 nm nanocrystals of Y_2O_2S.

Er^{3+} ions nonradiatively relax from the initially excited $^4F_{7/2}$ state to the $^4S_{3/2}$ metastable state via the intermediate levels of the $^2H_{11/2}$ multiplet. These phonons may then be absorbed by the Er^{3+} ions in the lowest level of the ground state to populate the upper levels of the $^4I_{15/2}$ ground state within a time much less than 5 ns so that optical excitation can be induced by the same laser pulse. As listed in Table 1, the energy level structure of Er^{3+} enables a 3-phonon relaxation from the $^4F_{7/2}$ state to the $^2H_{11/2}$ levels with single phonon energy approximately from 400 to 460 cm^{-1}, and from the $^2H_{11/2}$ levels to the $^4S_{3/2}$ levels with single phonon energy from 230 to 240 cm^{-1}. These phonons promote nearly resonant transition of Er^{3+} ions from the ground level into the upper levels of the $^4I_{15/2}$ ground state. In other words, phonon-participated cross-relaxation may occur in a number of channels without energy mismatch. The cross-relaxation processes are illustrated in Fig. 7. Another possible thermalization path is through phonon scattering due to lattice anharmonic effect. In such effect, high-energy phonons are annihilated for simultaneously creating multiple low-energy phonons with allowed energies of the lattice modes, and thus thermally excite Er^{3+} ions from the ground level to upper levels. Moreover, the upper electronic levels of $^4I_{15/2}$ can also be effectively populated through indirect Orbach process [17–19]. All these thermalization processes may occur within the 5 ns time period of the laser pulse, thus once an Er^{3+} ion at the intrinsic site is thermally excited into one of the

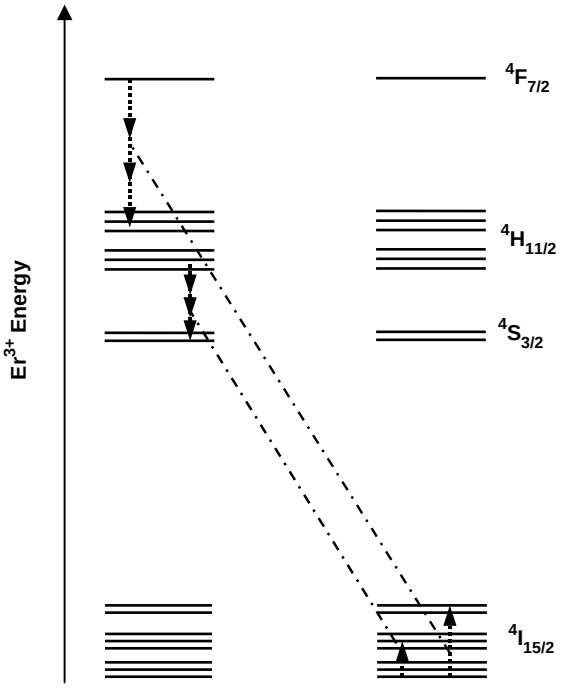

Fig. 7. Illustration of phonon cross-relaxation after laser induced excitation of Er^{3+} into the $^4F_{7/2}$ excited state.

upper levels, it may be excited by the laser pulse into the $^7F_{7/2}$ excited state. The observed hot bands are a result of competition between thermalization and relaxation.

Now we understand that for nanoparticles at low temperatures, direct phonon processes (emission or

absorption) are eliminated for the electronic energy gaps that are less than the cutoff phonon energy. The equilibrium population in the upper levels of $^4I_{15/2}$ results primarily from the competition between the 2-phonon Raman process (de-populating) and the laser induced thermalization (LIT) process (populating). In general, the 2-phonon Raman emission rate is approximately proportional to T^a ($a = 3 \sim 7$) [2], which can be numerically calculated once the PDOS is known. The LIT rate depends on pumping laser intensity, and weakly depends on temperature. When temperature is below 7 K, the 2-Phonon Raman emission rate is comparatively weak, so that the Er^{3+} population in the upper level is accumulated due to LIT process. Above 7 K, the 2-phonon Raman process becomes stronger and dominant. At higher temperatures, more phonon modes become active, and the direct phonon processes dominate the thermodynamics.

4.3. Evaluation of the anomalous thermalization effect

Based on the proposed mechanisms, we now present a simple model to evaluate the anomalous thermalization phenomenon observed in Er^{3+}:Y_2O_2S nanocrystals. With a simple rate-equation approach, it is reasonable to assume that below 70 K most Er^{3+} ions occupy the first three levels of $^4I_{15/2}$ (1,2,3 as marked in Fig. 1), since the energy gap between the levels 3 and 4 of $^4I_{15/2}$ is larger than 150 cm^{-1}. The laser-induced luminescence dynamics in Er^{3+}:Y_2O_2S nanocrystals can be described by the following set of rate equations:

$$\begin{aligned}
\frac{dN_1}{dt} &= -[b_2W_{21} + b_3W_{31} + (1-\beta_1)W_{LIT}]N_1 \\
&\quad + W_{21}N_2 + W_{31}N_3, \\
\frac{dN_2}{dt} &= (b_2W_{21} + \beta_2 W_{LIT})N_1 - W_{21}(1+b_2)N_2 + W_{21}N_3, \\
\frac{dN_3}{dt} &= (b_3W_{31} + \beta_3 W_{LIT})N_1 + b_2W_{21}N_2 \\
&\quad - (W_{21} + W_{31})N_3 N_1 + N_2 + N_3 = 1,
\end{aligned} \tag{4}$$

where the relative population on the levels are denoted by N_1, N_2 and N_3, respectively; and W_{if} ($= W_{if,\,1phonon} + W_{if,\,Raman}$) is the probability of phonon transition from level i to level f that include the contributions from residual single phonon emission ($W_{if,\,1phonon}$) and 2-phonon Raman emission process ($W_{if,\,Raman}$). The emission rates of direct process and 2-phonon Raman process between the Stark levels (1,2,3) can be calculated using the perturbation theory of electron–phonon interaction [18,19]. Here in the nanoparticle case, we replaced the ideal Debye continuous PDOS with the actual PDOS in the 20 nm sample that we calculated using Eqs. (1) and (2). Numerical calculation shows that, the ratio of 2-phonon Raman absorption rate to emission rate between level i and level j can be approximately expressed by the Boltzmann factor, $\exp(-\Delta E_{ij}/kT)$, the same is for the ratio of direct phonon absorption rate to emission rate. Therefore, in Eq. (4), we have $b_i \equiv W_{1i,\,absorption}/W_{i1,\,emission} = \exp(-\Delta E_{i1}/kT)$ ($i = 2, 3$). Because of the nearly equal gap among levels 1, 2 and 3, it is reasonable to assume $W_{32} = W_{21}$.

At relatively low laser intensity on the surface of the samples, we assume the equivalent populating rate of the laser induced thermalization (W_{LIT}) is linearly proportional to the pump laser intensity and the multiphonon relaxation rate (W_{NR}) from $^4F_{7/2}$ (W_{NR1}) and $^2H_{11/2}$ (W_{NR2}). That is

$$W_{LIT} = k_0 \frac{\sigma I_p}{h\nu_p} W_{NR}, \tag{5}$$

where

$$\begin{aligned}
W_{NR} &= W_{NR1} + W_{NR2}, \\
W_{NR1} &= W_{10}[1 - \exp(-410/kT)]^{-3}, \\
W_{NR2} &= W_{20}[1 - \exp(-240/kT)]^{-3},
\end{aligned}$$

k_0 is a scaling factor; I_p is the incident pump intensity; σ is the average absorption cross-section of the pump laser. For $T < 70$ K, W_{NR} is weakly dependent on temperature. The phonon energies released from multiphonon relaxation can be nearly resonantly absorbed by the Er^{3+} in the ground Stark level to level 8 at 410 cm^{-1} and level 6 at 249 cm^{-1}. Those ions then immediately relax to low-lying levels (Orbach process) and populate the lowest three levels of ground states. Based on the experiment observations, the branching ratios of the LIT rate from upper levels (6 and 8) to 1, 2, 3 are assumed to be 1:2:3. That is, $\beta_1 = 1/6$, $\beta_2 = 1/3$, $\beta_3 = 1/2$. In condition of thermal equilibrium, Eq. (4) can be solved by:

$$\begin{pmatrix} N_1 \\ N_2 \\ N_3 \end{pmatrix} = \begin{pmatrix} -[b_2W_{21} + b_3W_{31} + (1-\beta_1)W_{LIT} & W_{21} & W_{31} \\ b_3W_{31} + \beta_3 W_{LIT} & b_2W_{21} & -W_{21} - W_{31} \\ 1 & 1 & 1 \end{pmatrix}^{-1} \cdot \begin{pmatrix} 0 \\ 0 \\ 1 \end{pmatrix}. \tag{6}$$

The corresponding fluorescent intensities excited from levels 1–3 are known as

$$I_1 \propto \frac{\sigma_1 I_p}{h\nu_p} N_1, \quad I_2 \propto \frac{\sigma_2 I_p}{h\nu_p} N_2, \quad I_3 \propto \frac{\sigma_3 I_p}{h\nu_p} N_3, \tag{7}$$

where σ_1, σ_2, and σ_3 are the absorption cross-sections of the pump laser at 20,333, 20,310 and 20,288 cm^{-1}, respectively. Finally the temperature and power dependences of the normal line and hot bands can be numerically computed with Eqs. (3)–(7) and compared with the experiment. The calculated temperature dependence of the excitation spectra for $^4I_{15/2}(1,2,3) \rightarrow {}^4F_{7/2}(a)$ under the pump intensities of 60 and 5 kW/cm^2 on Er^{3+}:Y_2O_2S nanocrystals are shown by the solid curves in Fig. 3(a–c). The calculated curves indeed show a transition temperature near 7 K and saturation tendency below 5 K. Whereas the experimental results below transition temperature are well explained by the proposed mechanisms, at temperatures above the transition point, the calculated results show some differences from the experimental data. For instance, from 9 to 30 K, the calculated intensities of hot bands are somehow lower than the experimental results as shown in Fig. 3(b) and (c), and correspondingly the calculated normal band at 20,333 cm^{-1} is higher than the experimental results as shown in Fig. 3(a). This discrepancy may be due to the assumptions that we made for simplifying the calculations. Actually, there are many additional mechanisms, such as inelastic phonon scattering that influences the observed effects, but is not considered in our calculations. These mechanisms could be strongly dependent on the temperature and pump intensity. All the parameters used in the evaluation are summarized in Table 2. If we further assume that Er^{3+} population in level 3 is negligible, or for the $^4S_{3/2}$ excited state in which there are only two Stark levels, the ratio of the equilibrium Er^{3+} population in the upper and lower levels may be estimated as

$$\frac{N_2}{N_1} \approx e^{-\Delta E_{21}/kT} + \frac{W_{LIT}}{W_{21}} \tag{8}$$

N_2/N_1 expressed in Eq. (8) has the same temperature dependence as that is evaluated from Eq. (6), whereas the trend is very clear. At low temperature, the second term dominates, and at high temperature, the first term dominates.

The calculated intensity of the excitation spectra for $^4I_{15/2}(1,2,3) \rightarrow {}^4F_{7/2}(a)$ versus the pump intensity is compared with the experiments at 3 K, 20 K as shown in Fig. 4(a–b). At 3 K, as depicted in Fig. 4(a), the calculated intensities of the hot bands exhibit a nonlinear dependence on the pump laser intensity that fits to the experimental data with the power index of approximately 1.6 and 1.4 for laser intensity below and above 12 kW/cm^2, respectively. The excitation at 20,333 cm^{-1} clearly shows a saturation tendency with the increase of pump intensity, and its power index is approximately 0.9 and 0.6 for laser intensity below and above 12 kW/cm^2, respectively. Some differences between the calculated and experimental at low power are obvious and understandable, based on the same reason mentioned above. At 20 K, the calculated curves (Fig. 4b) show excellent agreement with the experimental results, which exhibit a linear dependence on the pump intensity.

Table 2
Parameters for fluorescence dynamics of Er^{3+} in Y_2O_2S nanocrystals

k_0 (s)	σ (cm^2)	W_{NR}[a] (s^{-1})	$W_{21}(0)$[a] (s^{-1})	$W_{31}(0)$[a] (s^{-1})
6.67×10^{-5}	4×10^{-20}	5×10^8	1×10^8	1.5×10^8

[a] Fixed value of spontaneous phonon emission rate at 0 K.

5. Conclusions

Because of the absence of low-frequency phonon modes in nanocrystals, the influence of ion-lattice interactions on optical spectroscopy and luminescence dynamics has been demonstrated to be significantly different from that in bulk materials. The anomalous thermalization phenomena that we observed in Er^{3+} doped Y_2O_2S nanocrystals with an average diameter of 20 nm have been analyzed using nonradiative phonon relaxation theory and calculated phonon density of state in 20 nm crystals. It is shown that although no quantum confinement should occur because of the localized electronic states, the optical spectrum and luminescence dynamics of an impurity ion in dielectric nanoparticles can be significantly modified through electron–phonon interaction. The anomalous thermalization phenomena, which were not observed in the Er^{3+}:Y_2O_2S bulk counterparts, can be well explained in the theoretical framework of ion-lattice interaction with consideration of confinement on phonon density of states.

Whereas the confinement effect on the appearance of hot bands in low-lying crystal field levels is significant only at temperature below 7 K for Er^{3+} ions in 20 nm nanocrystals, this phenomenon should occur at higher temperatures in smaller nanocrystals. Moreover, the confinement on electron–phonon interaction in nanocrystals is expected to induce more impacts to the luminescence dynamics of rare earth ions, which involve the low energy phonon modes of the lattice. These impacts includes, for instance, phonon assisted energy transfer and upconversion processes.

Acknowledgments

Work at Argonne National Laboratory was performed under the auspices of DOE Office of Basic Energy Sciences, Division of Chemical Sciences under contract No. W-31-109-ENG-38.

References

[1] G.K. Liu, H.Z. Zhuang, X.Y. Chen, Nano Lett. 2 (2002) 535.
[2] R.S. Meltzer, K.S. Hong, Phys. Rev. B 61 (2000) 3396.
[3] R.S. Meltzer, W.M. Yen, H. Zheng, S.P. Feofilov, M.J. Dejneka, B.M. Tissue, H.B. Yuan, Phys. Rev. B 64 (2001) 100201.
[4] H.S. Yang, S.P. Feofilov, D.K. Williams, J.C. Milora, B.M. Tissue, R.S. Meltzer, W.M. Dennis, Physica B 263–264 (1999) 476.
[5] R.S. Meltzer, S.P. Feofilov, B. Tissue, H.B. Yuan, Phys. Rev. B 60 (1999) R14012.
[6] H.S. Yang, K.S. Hong, S.P. Feofilov, B.M. Tissue, R.S. Meltzer, W.M. Dennis, J. Lumin. 83–84 (1999) 139.
[7] B.M. Tissue, Chem. Mater. 10 (1998) 2837.
[8] A. Tamura, K. Higeta, T. Ichinokawa, J. Phys. C 15 (1982) 4975; A. Tamura, Phys. Rev. B 52 (1995) 2688.
[9] C.R. Bickmore, K.F. Waldner, D.R. Treadwell, R.M. Laine, J. Am. Ceram. Soc. 79 (1996) 1419.
[10] C.B. Bickmore, K.F. Waldner, R. Baranwal, T. Hinklin, R.M. Laine, J. Eur. Ceram. Soc. 18 (1998) 287.
[11] J. Rossat-Mignod, J.C. Souillat, C. Linares, J. Phys. Chem. Solids 34 (1973) 371.
[12] W.T. Carnall, P.R. Fields, R. Sarup, J. Chem. Phys. 57 (1972) 43.
[13] M.F. Joubert, S. Guy, B. Jacquier, Phys. Rev. B 48 (1993) 10031.
[14] G.K. Liu, Y.H. Chen, J.V. Beitz, J. Lumin 81 (1999) 7.
[15] H. Lamb, Proc. Math. Soc. London 13 (1882) 187.
[16] C.A. Morrison, R.P. Leavitt, in: K.A. Gschneidner, L. Eyring (Eds.), Handbook on the Physics and Chemistry of Rare Earths, Vol. 5, North-Holland, Amsterdam, 1982, p. 584 (Chapter 46).
[17] T. Miyakawa, D.L. Dexter, Phys. Rev. B 1 (1970) 2961.
[18] R.C. Powell, Physics of Solid-state Laser Materials, Springer-Verlag, New York, 1998 (Chapter 4).
[19] B. Di Bartolo, Optical Interaction in Solids, Wiley, New York, 1968 (Chapter 15).